Neurosphere Segmentation in Brightfield Images

Jierong Cheng[a], Wei Xiong[a], Shue Ching Chia[a], Joo Hwee Lim[a], Shvetha Sankaran[b], and Sohail Ahmed[b]

[a]Institute for Infocomm Research, 1 Fusionopolis Way, Singapore 138632;
[b]Institute of Medical Biology, 8A Biomedical Grove, Singapore 138648

ABSTRACT

The challenge of segmenting neurospheres (NSPs) from brightfield images includes uneven background illumination (vignetting), low contrast and shadow-casting appearance near the well wall. We propose a pipeline for neurosphere segmentation in brightfield images, focusing on shadow-casting removal. Firstly, we remove vignetting by creating a synthetic blank field image from a set of brightfield images of the whole well. Then, radial line integration is proposed to remove the shadow-casting and therefore facilitate automatic segmentation. Furthermore, a weighted bi-directional decay function is introduced to prevent undesired gradient effect of line integration on NSPs without shadow-casting. Afterward, multiscale Laplacian of Gaussian (LoG) and localized region-based level set are used to detect the NSP boundaries. Experimental results show that our proposed radial line integration method (RLI) achieves higher detection accuracy over existing methods in terms of precision, recall and F-score with less computational time.

Keywords: Brightfield image, neurosphere segmentation, radial line integration, shadow casting, weighted bi-directional decay

1. INTRODUCTION

Neural stem cells (NSCs) and neural progenitors (NPs) generate the main phenotypes of the nervous system and have the potential to differentiate into neurons and glial cells.[1] Fluorescent microscopy cannot be used in the study of the effects of drugs on NSCs/NPs under different experimental variables, in which NSCs/NPs are killed because of the exposure to fluorescence light. Neurospheres (NSPs), free floating clustered of NSCs/NPs cultured in vitro, provide a method to investigate neural precursor cells in vitro.[2] Brightfield microscopy, as a non-fluorescent imaging modality, is an alternative for high content analysis of NSP formation.

One of the major challenges of brightfield cell images segmentation is caused by the uneven illumination throughout the field. Severe vignetting can be observed, in which the outer edges of the image are significantly darker than the center (Fig. 1(a)). Although vignetting could be effectively eliminated through the use of a corrective blank field,[3] a completely clean blank image on a microscope slide is not always available. Another problem emerged when raw site images are stitched together and illumination on the two sides of the seam is very different. The contrast in the center of the well is sufficient but becomes much lower near the well wall. Standard segmentation methods such as level sets,[4–6] which work well for fluorescent image segmentation, are not directly applicable on brightfield images[7] due to the poor image quality. Methods proposed for segmenting bright-field images include watershed and active contour techniques,[8] spectral K-Means approach,[9] textural segmentation,[10],[11] and local phase and active contours.[12] Methods in[8–10] require manual initialization while[12] requires multiple slices at different levels of defocus.

We observed that NSPs close to the well wall exhibit a shadow-casting appearance similar to cells in typical differential interference contrast (DIC) images: the fringe facing the well center appears dark and the fringe facing the well wall appears bright. None of the previous methods mentioned above have directly handled the shadow-casting effect in brightfield images. In this work, we use the line integration technique[13] in radial directions to eliminate the shadow-casting effect near the wall. During radial line integration, we proposed a weighted bi-directional decay function to prevent the undesired gradient effect. NSP detection is then performed by using multiscale Laplacian of Gaussian filtering and localized region-based level set.

Further author information:
Jierong Cheng: E-mail: chengjr@i2r.a-star.edu.sg, Telephone: +65 6408 2439

2. METHOD

2.1 Preprocessing

First of all, a region of interest (ROI) within each well is detected by applying Hough transform on the full well image. The center and radius of the ROI are thereby determined.[7]

Let $\{I_o^1, I_o^2, ..., I_o^n\}$ be the set of the stitched gray scale brightfield images of the whole well. The dimensions of the stitched images and the location of the seams are the same in all images. We create a synthetic blank field image I_b (Fig. 1(b)) by taking the median value of all the pixels on the same $(x, y) \in \mathbb{R}^2$ position from these images. The original images are then divided by this blank field image to remove the uneven illumination.

$$I_b(x, y) = \text{median}(I_o^1(x, y), I_o^2(x, y), ..., I_o^n(x, y)), \tag{1}$$

$$I^i(x, y) = I_o^i(x, y)/I_b(x, y), i = 1, 2, ..., n. \tag{2}$$

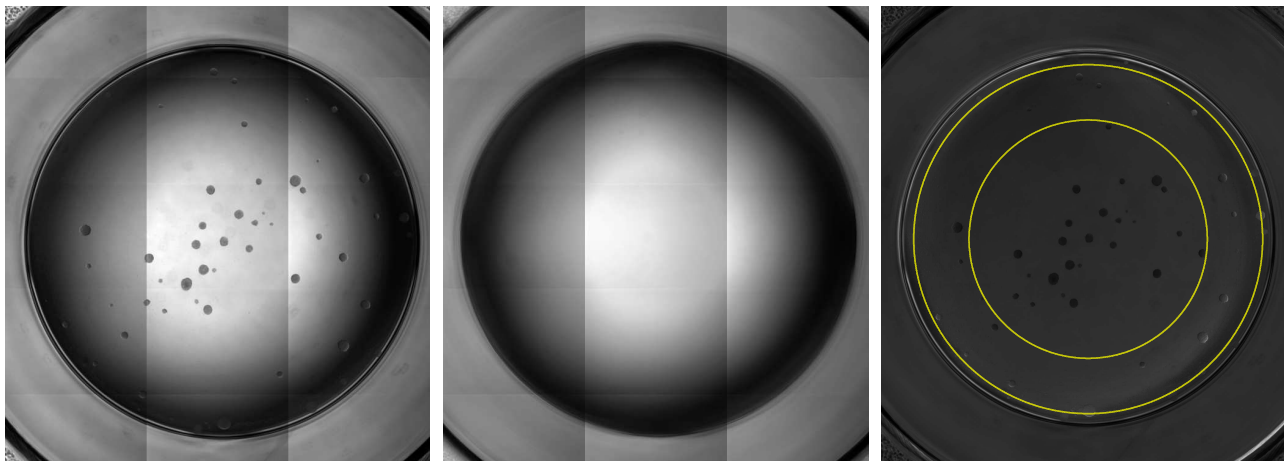

(a) (b) (c)

Figure 1. (a) Original brightfield image, (b) synthetic blank field image, and (c) image obtained by dividing (a) by (b). R^2 is the region bounded by the two yellow circles.

The pre-processing result is shown in Fig. 1(c), in which vignetting and illumination variation between different site images are greatly reduced. However, the contrast and appearance of NSPs still differ in accordance with their distance from the well center. Therefore, we choose to segment different regions in the whole well images separately. Let $\mathtt{c} = (\mathtt{c}_x, \mathtt{c}_y)$ and $\mathtt{r}$ be the center and the radius of a well respectively, the aforementioned ROI is divided into three regions after preprocessing: $R^1 = \{(x, y) \in \mathbb{R}^2 : \text{dist}(x, y; \mathtt{c}) < 0.8\mathtt{r}\}$, $R^2 = \{(x, y) \in \mathbb{R}^2 : 0.65\mathtt{r} < \text{dist}(x, y; \mathtt{c}) < 0.95\mathtt{r}\}$, and $R^3 = \{(x, y) \in \mathbb{R}^2 : 0.9\mathtt{r} < \text{dist}(x, y; \mathtt{c}) < \mathtt{r}\}$ where $\text{dist}(x, y; \mathtt{c})$ is the Euclidean distance from (x, y) to $\mathtt{c}$. The NSPs in R^2 where shadow-casting appears (see Fig. 1(c)) are detected by the radial line integration and multiscale LoG based method described in Sections 2.2 and 2.3. In R^1 and R^3, the contrast between the NSPs and the background is relatively sufficient and constant, so NSPs are detected later without shadow-casting removal. R^1, R^2, and R^3 are slightly overlapped to ensure that NSPs lying on the region borders are detected. We take the union of the binary images representing segmentation results from the three regions as the final result.

2.2 Shadow-casting removal

An image $\tilde{I}$ is created by convert the preprocessed image I from Cartesian to Polar coordinate system. The pole of the polar coordinate system is the well center pre-determined.

$$\tilde{I}(\rho, \theta) = I(x, y), \quad (x, y) \in R^2 \tag{3}$$

where

$$\rho = \sqrt{(x - \mathtt{c}_x)^2 + (y - \mathtt{c}_y)^2} - 0.65\mathtt{r}, \quad \rho \in [0, w] \tag{4}$$

$$\theta = \arctan((y - \mathtt{c}_y)/(x - \mathtt{c}_x)), \quad \theta \in [0, 2\pi). \tag{5}$$

The width of $\tilde{I}$ is $w = 0.95\mathtt{r} - 0.65\mathtt{r} = 0.3\mathtt{r}$. In $\tilde{I}$ (Fig. 2(a)), we observe that the shadow-casting on B-labeled NSPs near the vertical center of the image ($\rho = \frac{1}{2}w$) is more serious than those A-labeled near the left/right border ($\rho = 0/w$).

To create a more or less 'flat' background, the low frequency image components are subtracted by high-pass filtering. In Fourier domain, an ideal high-pass filter sets all frequencies inside a circle to zero while passing all frequencies outside the circle. We set the radius of the circle (cutoff frequency) to be 0.02 times the highest radian frequency of the image. The ideal high-pass filter is smoothed by an average filter of 7×7 to reduce the ringing effect. The Fourier transform of $\tilde{I}$ is multiplied by the high-pass filter and then undergos inverse Fourier transform to give a high-pass filtered image I_{hp}.

Kam proposed to use line integration to computationally invert the directional gradient performed by DIC imaging.[13] For usual DIC images, the integration is performed at a shear angle of 45 degree. For our Polar-transformed brightfield images, we need to integrate them along the $\Delta\rho$ (horizontal) direction, i.e. the radial direction in original brightfield image. Randomly distributed striped structure prevails, which is caused by the accumulation of noise along the integration path and the inclusion of slowly-varying image components. We suppress this effect by incorporating an exponential decay factor and integrating along two opposite paths (bi-directional decay):

$$J_1(\rho, \theta) = \int_0^{\rho} \int_{\theta - d}^{\theta + d} I_{hp}(s, t) \exp\left(\frac{s - \rho}{s_0}\right) \mathrm{d}s\mathrm{d}t, \tag{6}$$

$$J_2(\rho, \theta) = \int_{\rho}^{w} \int_{\theta - d}^{\theta + d} I_{hp}(s, t) \exp\left(\frac{\rho - s}{s_0}\right) \mathrm{d}s\mathrm{d}t, \tag{7}$$

where s_0 is a constant coefficient and $d = 1$ determines the degree of averaging along the $\Delta\theta$ direction.

Since the decay factor introduces asymmetry on the integration path, $(J_1 - J_2)$ can be taken to generate a new image,[13] which works for B-labeled NSPs. However, for those NSPs without shadow-casting originally, this operation creates gradient effect similar to shadow-casting. For example in Fig. 2(b), A-labeled NSPs show a bright left fringe and a dark right fringe or vice versa. This effect will interfere with the following blob detection (we will explain it later in Section 2.3). To prevent the undesired gradient effect, we propose to a new method: we apply the bi-directional decay only near ($\rho = \frac{1}{2}w$) where shadow-casting is obvious in the original image; whereas we use single-directional decay near the left/right border ($\rho = 0/w$). Formally, this bi-directional decay is weighted by ρ, defined by

$$J(\rho, \theta) = 2\left(\frac{w - \rho}{w} J_1(\rho, \theta) - \frac{\rho}{w} J_2(\rho, \theta)\right), \tag{8}$$

which leads to

$$J(\rho, \theta) \to \begin{cases} 2J_1(\rho, \theta) & \text{when} \quad \rho \to 0 \\ J_1(\rho, \theta) - J_2(\rho, \theta) & \text{when} \quad \rho \to \frac{1}{2}w \\ -2J_2(\rho, \theta) & \text{when} \quad \rho \to w. \end{cases} \tag{9}$$

Fig. 2(c) illustrates the results of applying Eqn. (8). Compared to Fig. 2(a), we find the shadow-casting on B-labeled NSPs is eliminated and the intensities within cells are generally lower than the background. Compared to Fig. 2(b), no gradient effect is found on A-labeled NSPs.

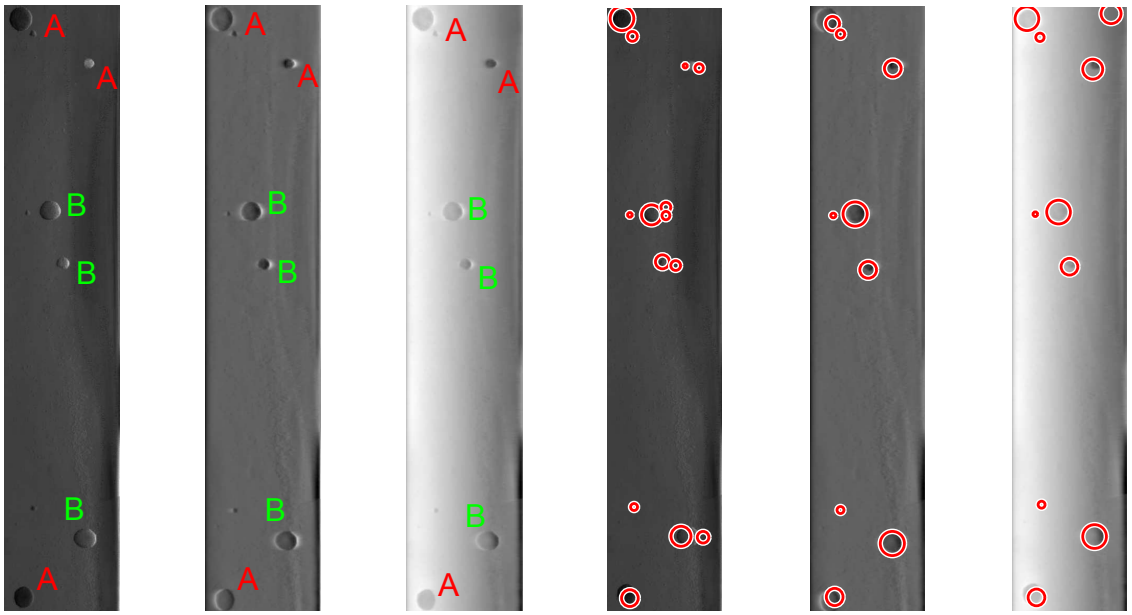

(a) (b) (c) (d) (e) (f)

Figure 2. (a) Cropped polar-transformed image ($\tilde{I}$). Horizontal axis: $\rho \in [0, w]$, vertical axis: $\theta \in [0, 0.77\pi]$. (b) Bi-directionally decayed image ($J_1 - J_2$). (c) Weighted bi-directionally decayed image (J). (d) Blob detection result on (a). (e) Blob detection result on (b). (f) Blob detection result on (c).

2.3 NSP detection and segmentation

In order to detect the NSPs in radial line-integrated images, we propose to use a multiscale Laplacian of Gaussian (LoG) described by Lindeberg[14] for blob detection. The LoG filtering is an effective tool for estimating the cell size and the location without explicit segmentation. A three-dimensional discrete scale space $L(\rho, \theta, \sigma^2)$ defined by the three parameters is created by convolving an two-dimensional image with scale-normalized LoG kernels of different sizes:

$$L(\rho, \theta, \sigma^2) = J(\rho, \theta) * \sigma^2 \nabla^2 G_\sigma(\rho, \theta) \tag{10}$$

where ∇^2 is the Laplacian operator and $G_\sigma(\rho, \theta)$ is a two-dimensional Gaussian kernel of standard deviation σ. The filtering results in strong positive responses for dark blobs and strong negative responses for bright blobs. The responses across all scales are maximum/minimum at the center of each object with radius equal to $\sqrt{2}\sigma$. To capture NSPs of various size, a multiscale approach is adopted: σ is set to be increasing proportionally from $\sigma_{\min} = 2$ to $\sigma_{\max} = 28$. A point $(\hat{\rho}, \hat{\theta}; \hat{\sigma}^2)$ is regarded as the center of a dark blob if the value of L at this point is greater than those values in all its 26 neighbors. Each local maximum in this scale space identifies a candidate cell with its location, size, and filter responses known. The abundance of candidates is pruned according to three criteria. First, candidates with a value of response higher than a threshold t_2 are discarded. Second, candidates with any part of their boundaries outside R^2 are removed. Finally, only the largest candidates among a group of overlapped candidates remain.

The NSPs detected from the weighted bi-directionally decayed image are shown as circles in Fig. 2(f). The center of a circle $(\hat{\rho}, \hat{\theta})$ is the point at which the spatial maximum is assumed. The radius is set to be $\sqrt{2}\hat{\sigma}$ where $\hat{\sigma}$ is the scale at which the maximum is assumed. When applied on simply polar-transformed image, it often detects multiple side-by-side blobs on B-labeled NSPs due to shadow-casting (Fig. 2(d)). As for bi-directionally decayed image, gradient effect on A-labeled NSPs causes improper size estimation (Fig. 2(e)). The most accurate blob detection is obtained from the weighted bi-directionally decayed image.

The final NSPs boundary is obtained by applying Lankton's localized region-based level set[15] to the radial line-integrated image. To reduce the computational time, we apply the localized level set in a multiscale way instead of using a large radius directly on the original-scaled image. We use a relatively small radius to start

with the coarsest re-scaled image (scale = 0.25) and then use the converged contours to initialize the level set in the next finer scale (scale = 0.5). The same procedure repeats until the contour converges in the original scale (scale = 1).

3. RESULTS

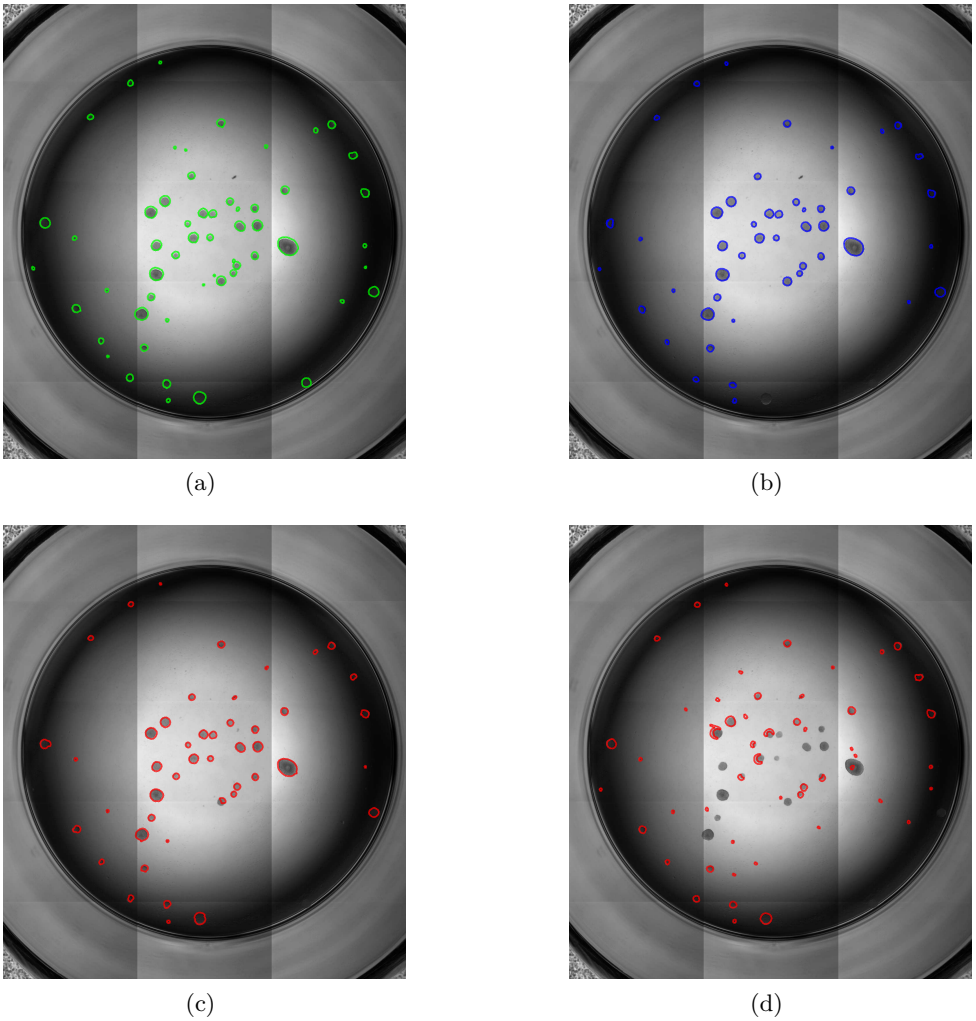

(a) (b) (c) (d)

Figure 3. (a) Ground truth of NSP positions and segmentation results by (b) radial line integration, (c) localized level set, and (d) sparseness-enhanced multiplicative update.

Neural stem cells (NSCs) are cultivated in multi-well plates with images captured under brightfield microscopy at 4X magnification. Each well is covered by 15 imaging sites in a configuration arranged in 3 columns by 5 rows. After stitching together 15 imaging sites, the size of each well image is 1730×1392 pixels. In our experiments, we use 32 wells covered by 480 site images which consists of 738 NSPs. The ground truth is obtained from fluorescence images and manually verified by biologists. Our experiments are implemented in Matlab R2012a on a machine with 3.2GHz CPU and 12GB RAM.

The parameters used in our method are listed in Table 1. Besides, the level set parameters are set as follows: number of iterations = 100, localization radius = 9, weight of smoothing term = 0.2, and convergence threshold = 0.02. All of the parameter values are determined empirically.

Table 1. List of parameter settings in R^1, R^2, and R^3.

Region	Description	Value
R^2	*Integration coefficient*	$s_0 = 5$
$R^1 \cup R^2 \cup R^3$	*LoG response threshold*	$t = 2.0$
	Criterion of NSP shape	eccentricity < 0.85
	Criterion of NSP size	area > 40

Table 2. Quantitative evaluation and comparison result (RLI: proposed radial line integration method; LLS: localized level set; SEMU: sparseness-enhanced multiplicative update).

	Precision (%)	Recall (%)	F-score (%)	Time
RLI	**95.73**	82.11	**88.40**	92 s
LLS	89.13	**82.25**	85.55	137 s
RLI (R^2)	**94.27**	**83.49**	**88.55**	
LLS (R^2)	88.24	80.95	84.44	
SEMU (R^2)	82.20	76.51	79.54	

Precision, recall, and F-score are used to evaluate the detection accuracy of our proposed method, defined as follows

$$\text{precision} = \frac{TP}{TP + FP}, \quad \text{recall} = \frac{TP}{P}, \quad \text{F-score} = \frac{2TP}{P + TP + FP},$$

where TP is the number of true positives, FP is the number of false positives, and P is the number of NSPs in ground truth. We compare our radial line integration based method (RLI) with a localized level set method (LLS)[7] previously published by our group. RLI achieved higher precision and F-score, and cost less computational time than LLS (see Table 2). We also compare the accuracy in R^2 with the sparseness-enhanced multiplicative update (SEMU) algorithm.[16] SEMU was proposed for preconditioning microscopy images to deal with shadow-casting artifacts in DIC images. Therefore, it is not appropriate to compare to the results of SEMU in R^1 and R^3 where shadow-casting does not exist. In R^2, RLI has the leading precision, recall and F-score among the three methods. The ground truth and segmentation results of one well are shown in Fig. 3.

4. CONCLUSIONS

We have proposed a vignetting and shadow removal method for neurosphere segmentation in brightfield images. After removing vignetting by creating a synthetic blank field image, a line integration algorithm is applied on the radial transformed image to remove the shade-casting effect. Furthermore, a weighted bi-directional decay function proves effective for preventing undesired gradient effect during the process. Blob detection by multiscale LoG filtering provides initialization for localized region-based level set. The detection accuracy in terms of precision, recall, and F-score has been improved notably compared to existing methods. Our future work will focus on the improvement of boundary accuracy near the well wall.

ACKNOWLEDGMENTS

We thank Lee Hwee Kuan for helpful discussions. This work is supported in part by Agency for Science, Technology and Research, Joint Council Office (Grant number JCOAG03_FG01_2009).

REFERENCES

[1] Lois, C. and Alvarez-Buylla, A., "Proliferating subventricular zone cells in the adult mammalian forebrain can differentiate into neurons and glia," *Proc. Natl. Acad. Sci. USA* **90**(5), 2074–2077 (1993).

[2] Reynolds, B. A. and Weiss, S., "Clonal and population analyses demonstrate that an EGF-responsive mammalian embryonic cns precursor is a stem cell," *Developmental Biology* **175**, 1–13 (1996).

[3] Marty, G. D., "Blank-field correction for achieving a uniform white background in brightfield digital photomicrographs," *BioTechniques* **42**(6), 716–720 (2007).

[4] Chan, T. F. and Vese, L. A., "Active contours without edges," *IEEE Trans. Image Processing* **10**(2), 266–277 (2001).

[5] Vese, L. A. and Chan, T. F., "A multiphase level set framework for image segmentation using the mumford and shah model," *International Journal of Computer Vision* **50**, 271–293 (2002).

[6] Li, C.and Xu, C., Gui, C., and Fox, M. D., "Level set evolution without re-initialization: A new variational formulation," *Proc. CVPR*, 430–436 (2005).

[7] Xiong, W., Chia, S.-C., Lim, J.-H., Lee, H.-K., Sankaran, S., and Ahmed, S., "Segmentation of neural stem cells/neurospheres in high content brightfield microscopy images using localized level sets," *Proc. ICIP*, 2009–2012 (2012).

[8] Tse, S., Bradbury, L., Wan, J., Djambazian, H., Sladek, R., and Hudson, T., "A combined watershed and level set method for segmentation of brightfield cell images," *Proc. SPIE Medical Imaging* **7259**, 4748–4751 (2009).

[9] Bradbury, L. and Wan, J. W. L., "A spectral k-means approach to bright-field cell image segmentation," *Proc. EMBC*, 4748–4751 (2010).

[10] Korzynska, A., Strojny, W., Hoppe, A., Wertheim, D., and Hoser, P., "Segmentation of microscope images of living cells," *Pattern. Anal. Applic.* **10**(4), 301–319 (2007).

[11] Iwanowski, M. and Korzynska, A., "Detection of the area covered by neural stem cells in cultures using textural segmentation and morphological watershed," *Computer Recognition Systems 3, Advances in Intelligent and Soft Computing* **57**, 543–557 (2009).

[12] Ali, R., Gooding, M., Szilágyi, T., Vojnovic, B., Christlieb, M., and Brady, M., "Automatic segmentation of adherent biological cell boundaries and nuclei from brightfield microscopy images," *Machine Vision and Applications* **23**(4), 607–621 (2012).

[13] Kam, Z., "Microscopic differential interference contrast image processing by line integration (lid) and deconvolution," *Bioimaging* **6**(4), 166–176 (1998).

[14] Lindeberg, T., "Feature detection with automatic scale selection," *International Journal of Computer Vision* **30**(2), 79–116 (1998).

[15] Lankton, S. and Tannenbaum, A., "Localizing region-based active contours," *IEEE Trans. on Image Processing* **17**(11), 2029–2039 (2008).

[16] Li, K. and Kanade, T., "Nonnegative mixed-norm preconditioning for microscopy image segmentation," *Proc. IPMI*, 362–373 (2009).